CMS Physics Analysis Summary

Observation of $\gamma\gamma \to \tau\tau$ in proton-proton collisions and limits on the anomalous electromagnetic moments of the τ lepton

The CMS Collaboration

Abstract

The photon-induced production of a pair of τ leptons, $\gamma\gamma \to \tau\tau$, is observed for the first time in proton-proton collisions. The observation is based on a data set recorded with the CMS detector at the LHC at a center-of-mass energy of 13 TeV and corresponding to an integrated luminosity of 138 fb^{-1}. Events with a small number of tracks close to the di-τ vertex are selected to isolate photon-induced processes. Limits on the anomalous electromagnetic moments of the τ lepton originating from potential new physics effects on the $\gamma\tau\tau$ vertex are also set.

1 Introduction

The production of lepton pairs in photon-induced interactions draws significant interest since it is a pure quantum electrodynamics (QED) process, for which the cross section is known with a high level of accuracy. This process is characterized by its color-neutral nature, leading to low hadronic activity, and was first measured by the CMS Collaboration in the dielectron and dimuon final states [1, 2]. Although the photon-lepton vertex is measured up to high precision for electrons and muons, the couplings to τ leptons lack a similar experimental precision.

The most general form of photon-lepton vertex ($ie\Gamma^\mu$) satisfying Lorentz invariance is:

$$\Gamma^\mu = \gamma^\mu F_1\left(q^2\right) + \frac{\sigma^{\mu\nu} q_\nu}{2m}\left[iF_2\left(q^2\right) + F_3\left(q^2\right)\gamma_5\right],\qquad(1)$$

where F_1, F_2 and F_3 are form factors that contain the complete information about the lepton's gross electric and magnetic couplings. Beyond serving as a deep test of QED interactions, the photon-lepton vertex also offers insights into the anomalous electromagnetic moments of the lepton, $F_2\left(0\right) = a_\ell \equiv \left(g_\ell - 2\right)/2$ and $F_3\left(0\right) = -\frac{2m}{e}d_\ell$, and is a powerful probe of physics beyond the standard model (BSM). In this expression, the gyromagnetic ratio g_ℓ is a constant term that relates the magnetic moment to the spin of the lepton. The one-loop contribution to a_ℓ is equal to the so-called "Schwinger term" [3]:

$$a_\ell = \frac{\alpha}{2\pi} \simeq 0.00116,\qquad(2)$$

where α is the fine-structure constant.

The anomalous magnetic moment of the electron was measured to be in agreement with the standard model (SM) with an impressive precision of 12 significant digits [4, 5], whereas a tension of about 4 standard deviations (s.d.) with respect to the theoretical prediction was observed by the Muon g-2 Collaboration when measuring a_μ [6, 7]. If BSM effects scale with the squared lepton mass [8], deviations of a_τ from the SM predictions would be more than two orders of magnitude larger. The photon-induced production of a τ lepton pair involves $\tau\tau\gamma$ vertices and can be used to measure a_τ, which, in the SM, is predicted to be $a_\tau = 117721(5) \times 10^{-8}$ [9]. This same process can also be studied to constrain the electric dipole moment (EDM) of the τ lepton, d_τ, which, since there is no appreciable CP violation in the lepton sector in the SM [10], is predicted to have a nonzero but tiny value ($d_\tau = -7.3 \times 10^{-38}\,e\,\mathrm{cm}$).

The signal in this analysis is $\mathrm{pp}(\gamma\gamma) \to \mathrm{p}^{(*)}\tau^+\tau^-\mathrm{p}^{(*)}$, where $\mathrm{p}^{(*)}$ denotes a final state proton that stays intact or fragments after the photon emission. In the following, charges will be omitted from the notations for simplicity. When coherent photon radiation happens without proton dissociation for both photons, the process is called exclusive or elastic. Elastic photon emissions force the photons to be almost on-shell, limiting their virtuality to small values ($q^2 \to 0$) [11]. When one or two photons are radiated off a parton of the proton, the process is either single-dissociative or double-dissociative. The three diagrams are shown in Fig. 1. Single-dissociative and double-dissociative events can also give rise to an elastic-like signature when the proton remnants are not reconstructed because they fall outside of the detector acceptance.

The $\gamma\gamma \to \tau\tau$ process has been observed by the ATLAS and CMS experiments in ultraperipherical collisions of nuclei [12, 13], and further used to set constraints on a_τ. The observation was driven by signal events with a di-τ invariant mass, $m_{\tau\tau}$, typically below $20\,\mathrm{GeV}$. This note describes the first measurement of the photon-induced production of a pair of τ leptons in proton-proton (pp) collisions. Because of the trigger requirements, experimentally accessible
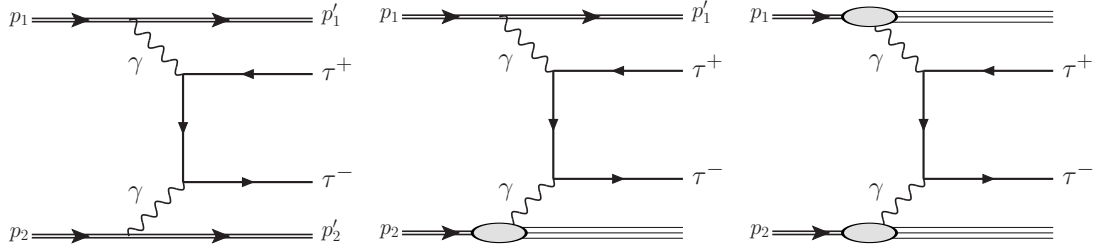
Figure 1: Production of τ lepton pairs by $\gamma\gamma$ fusion. The exclusive (left), single proton dissociation or semiexclusive (middle), and double proton dissociation (right) topologies are shown.

signal events have $m_{\tau\tau} > 50\,\text{GeV}$. This phase space has a much lower cross section, but the integrated luminosity is higher than that of the heavy ion runs. Additionally, BSM effects are enhanced at high mass, such that constraints on BSM scenarios with non-SM a_τ and d_τ values can be set using both the rate of the signal and its $m_{\tau\tau}$ distribution. Outside of LHC experiments, constraints on a_τ were previously set by the DELPHI, OPAL, and L3 experiments [14–16]. The best constraint on d_τ comes from the Belle experiment [17], while the ARGUS, OPAL, and L3 Collaborations also determined confidence intervals [15, 16, 18].

This note presents the first observation of the $\gamma\gamma \to \tau\tau$ process in pp collision events, as well as constraints on a_τ and d_τ. It is based on pp collision data at $\sqrt{s} = 13\,\text{TeV}$ collected with the CMS detector in 2016–2018 and corresponding to an integrated luminosity of $138\,\text{fb}^{-1}$. To select the signal, we apply so-called exclusivity criteria, which rely on the geometry of the di-τ system and on the activity in the tracker part of the detector around the di-τ vertex. In particular, selecting events with no track around the di-τ vertex can reduce the backgrounds by about three orders of magnitude for a signal efficiency around 50%. Such a strategy was used recently by the ATLAS experiment to observe $\gamma\gamma \to WW$ events in pp collisions [19], and in earlier searches and measurements at the LHC [2, 20–23]. Four different final states are used to extract the signal, depending on the decay of the τ lepton: $e\mu$, $e\tau_h$, $\mu\tau_h$, and $\tau_h\tau_h$, where τ_h denotes a τ lepton decaying hadronically. Events with two reconstructed muons are also used to derive corrections to the simulated samples. The visible mass of the τ candidates, m_{vis}, computed as the invariant mass of the visible decay products of the τ leptons, is used as a biased estimator of $m_{\tau\tau}$ to extract the significance of the signal and constraints on a_τ and d_τ.

2 The CMS detector

The central feature of the CMS apparatus is a superconducting solenoid of 6 m internal diameter, providing a magnetic field of 3.8 T. Within the solenoid volume are a silicon pixel and strip tracker, a lead tungstate crystal magnetic calorimeter (ECAL), and a brass and scintillator hadron calorimeter (HCAL), each composed of a barrel and two endcap sections. Forward calorimeters extend the pseudorapidity coverage provided by the barrel and endcap detectors. Muons are measured in gas-ionization detectors embedded in the steel flux-return yoke outside the solenoid. A more detailed description of the CMS detector, together with a definition of the coordinate system used and the relevant kinematic variables, can be found in Ref. [24].

Events of interest are selected using a two-tiered trigger system. The first level (L1), composed of custom hardware processors, uses information from the calorimeters and muon detectors to select events at a rate of around 100 kHz within a fixed latency of about 4 μs [25]. The second level, known as the high-level trigger (HLT), consists of a farm of processors running a version of the full event reconstruction software optimized for fast processing, and reduces the event rate to around 1 kHz before data storage [26].

3 Signal and background modeling

Signal samples corresponding to the elastic photon-induced production of a τ lepton pair are generated using the GAMMA-UPC generator [27], which handles final states produced via photon fusion incorporated in MADGRAPH5_AMC@NLO v3.5 [28–30]. Photon fluxes are derived from the integral over the charge form factors of the nucleus. The SUPERCHIC 4 generator [31] is used as a cross check, as described in Section 7.

In this analysis, a_τ and d_τ are parameterized using the SMEFTsim package [32, 33], as suggested in Ref. [8]. The corresponding BSM Lagrangian in the SM effective field theory (SMEFT) approach consists of two dimension-6 operators modifying a_τ and d_τ at tree level:

$$\mathcal{L}_{\text{BSM}} = \frac{C_{\tau B}}{\Lambda^2} \bar{L}_L \sigma^{\mu\nu} \tau_R H B_{\mu\nu} + \frac{C_{\tau W}}{\Lambda^2} \bar{L}_L \sigma^{\mu\nu} \tau_R \sigma^i H W^i_{\mu\nu} + \text{h.c.,} \tag{3}$$

where Λ is the scale of BSM physics and $C_{\tau B}$ and $C_{\tau W}$ are Wilson coefficients. Using the *SMEFTsim_general_alphaScheme_UFO* model, after electroweak symmetry breaking, the $\tau\tau\gamma$ vertex is parameterized as:

$$V_{\tau\tau\gamma} = ie\gamma^\mu - \frac{v\sqrt{2}}{\Lambda^2} \left[\text{Re}\left[C_{\tau\gamma}\right] + \text{Im}\left[C_{\tau\gamma}\right] i\gamma_5 \right] \sigma^{\mu\nu} q_\nu, \tag{4}$$

where v is equal to 246 GeV, $C_{\tau\gamma} = \left(cos\theta_W C_{\tau B} - \sin\theta_W C_{\tau W} \right)$, and θ_W is the Weinberg angle. Using Eq. (1) and Eq. (4), the BSM contributions to a_τ and d_τ can be expressed as:

$$\delta a_\tau = \frac{2m_\tau}{e} \frac{\sqrt{2}v}{\Lambda^2} \text{Re}\left[C_{\tau\gamma}\right] \tag{5}$$

and

$$\delta d_\tau = \frac{\sqrt{2}v}{\Lambda^2} \text{Im}\left[C_{\tau\gamma}\right]. \tag{6}$$

For simplicity and without loss of generality since δa_τ and δd_τ only depend on $C_{\tau\gamma}$ and not on the individual values of $C_{\tau W}$ and $C_{\tau B}$, we set $C_{\tau W}$ to 0 in the signal simulation. BSM contributions to the $Z \to \tau\tau$ vertex cancel for $C_{\tau W} = -\tan\theta_W C_{\tau B}$, but other values of $C_{\tau W}$ would result in variations in the Drell–Yan process prediction that are negligible with respect to the systematic uncertainties in this analysis. The analysis results can therefore be interpreted in the two-dimensional plane of $C_{\tau W}$ and $C_{\tau B}$. The simulation of different anomalous electromagnetic moments is performed using a matrix element reweighting [34], scanning over a range of $C_{\tau B}$ values. In the simulation we set Λ to 2 TeV, but the results were checked not to depend on the scale of new physics for $\Lambda > 0.5$ TeV since only the $C_{\tau W}/\Lambda^2$ and $C_{\tau B}/\Lambda^2$ ratios can be measured.

Single-dissociative and double-dissociative processes are not simulated but estimated from data as described later. The same generator is used to simulate the elastic photon-induced production of pairs of electrons, muons, and W bosons, which are backgrounds in the signal region (SR).

The MADGRAPH5_AMC@NLO 2.6.5 event generator is used to generate events originating from the Z/γ^* + jets and W + jets processes, as well as from the diboson production with two leptons and two neutrinos in the final state. They are simulated at next-to-leading order (NLO) with the FxFx jet matching and merging [30]. The MADGRAPH5_AMC@NLO generator is also used for the simulation of the minor contribution from other diboson production events, whereas

POWHEG 2.0 [35–39] is used for $t\bar{t}$ and single top quark production. The generators are interfaced with PYTHIA 8.240 [40] to model the parton showering, fragmentation, and hadronization, as well as the decay of the τ leptons. The PYTHIA parameters affecting the description of the underlying event are set to the CP5 tune [41]. The NNPDF3.1 parton distribution function (PDF) set [42–44] at next-to-NLO (NNLO) accuracy is used for background simulations. Additional pp interactions per bunch crossing (pileup, PU) are added to the simulated samples with a distribution that is chosen to match that observed in the data. Generated events are processed through a GEANT4 [45] simulation of the CMS detector.

4 Object reconstruction

The global event reconstruction (also called particle-flow event reconstruction [46]) aims to reconstruct and identify each individual particle in an event, with an optimized combination of all subdetector information. In this process, the identification of the particle type (photon, electron, muon, charged hadron, neutral hadron) plays an important role in the determination of the particle direction and energy. Photons (e.g., coming from π^0 decays or from electron bremsstrahlung) are identified as ECAL energy clusters not linked to the extrapolation of any charged particle trajectory to the ECAL. Electrons (e.g., coming from photon conversions in the tracker material or from B hadron semileptonic decays) are identified as a primary charged particle track and potentially many ECAL energy clusters corresponding to this track extrapolation to the ECAL and to possible bremsstrahlung photons emitted along the way through the tracker material. Muons (e.g., from B hadron semileptonic decays) are identified as tracks in the central tracker consistent with either a track or several hits in the muon system, and associated with calorimeter deposits compatible with the muon hypothesis. Charged hadrons are identified as charged particle tracks neither identified as electrons, nor as muons. Finally, neutral hadrons are identified as HCAL energy clusters not linked to any charged hadron trajectory, or as a combined ECAL and HCAL energy excess with respect to the expected charged hadron energy deposit.

The electron momentum is estimated by combining the energy measurement in the ECAL with the momentum measurement in the tracker. The momentum resolution for electrons with transevrse momentum $p_T \approx 45\,\text{GeV}$ from $Z \rightarrow$ ee decays ranges from 1.6 to 5%. It is generally better in the barrel region than in the endcaps, and also depends on the bremsstrahlung energy emitted by the electron as it traverses the material in front of the ECAL [47, 48].

Muons are measured in the pseudorapidity range $|\eta| < 2.4$, with detection planes made using three technologies: drift tubes, cathode strip chambers, and resistive plate chambers. The single muon trigger efficiency exceeds 90% over the full η range, and the efficiency to reconstruct and identify muons is greater than 96%. Matching muons to tracks measured in the silicon tracker results in a relative p_T resolution, for muons with p_T up to 100 GeV, of 1% in the barrel and 3% in the endcaps. The p_T resolution in the barrel is better than 7% for muons with p_T up to 1 TeV [49].

Hadronic τ decays (τ_h) are reconstructed from jets, using the hadrons-plus-strips algorithm [50], which combines 1 or 3 tracks with energy deposits in the calorimeters. Neutral pions are reconstructed as strips with dynamic size in η-ϕ from reconstructed electrons and photons, where the strip size varies as a function of the p_T of the electron or photon candidate. The τ_h are reconstructed in four possible decay modes (DMs): a single charged hadron ($h^\pm$), a charged hadron with at least one neutral pion ($h^\pm + \pi^0$(s)), three charged hadrons with no neutral pion ($h^\pm h^\mp h^\pm$), or 3 charged hadrons with at least one neutral pion ($h^\pm h^\mp h^\pm + \pi^0$(s)). To distinguish genuine τ_h decays from jets originating from the hadronization of quarks or gluons, and from

electrons, or muons, the DEEPTAU algorithm is used [51]. Information from all individual reconstructed particles near the τ_h axis is combined with properties of the τ_h candidate and the event. The rate of a jet to be misidentified as τ_h by the DEEPTAU algorithm depends on the p_T and quark flavor of the jet. In simulated events from W boson production in association with jets it has been estimated to be 0.43% for a genuine τ_h identification efficiency of 70%. The misidentification rate for electrons (muons) is 2.60 (0.03)% for a genuine τ_h identification efficiency of 80 (>99)%.

The missing transverse momentum vector $\vec{p}_T^{\,\mathrm{miss}}$ is computed as the negative vector sum of the transverse momenta (p_T) of all the PF candidates in an event, and its magnitude is denoted as p_T^{miss} [52]. The $\vec{p}_T^{\,\mathrm{miss}}$ is modified to account for corrections to the energy scale of the reconstructed jets in the event. Anomalous high-p_T^{miss} events can be due to a variety of reconstruction failures, detector malfunctions or noncollision backgrounds. Such events are rejected by event filters that are designed to identify more than 85–90% of the spurious high-p_T^{miss} events with a mistagging rate less than 0.1% [52].

Tracks with $p_T > 0.5\,\mathrm{GeV}$ and $|\eta| < 2.5$ are used in this analysis to measure the hadronic activity in the event. The silicon tracker used in 2016 measured charged particles within the range $|\eta| < 2.5$. For nonisolated particles of $1 < p_T < 10\,\mathrm{GeV}$ and $|\eta| < 1.4$, the track resolutions were typically 1.5% in p_T and 25–90 (45–150) μm in the transverse (longitudinal) impact parameter [53]. At the start of 2017, a new pixel detector was installed [54]; the upgraded tracker measured particles up to $|\eta| < 3.0$ with typical resolutions of 1.5% in p_T and 20–75 μm in the transverse impact parameter [55] for nonisolated particles of $1 < p_T < 10\,\mathrm{GeV}$.

During the 2016 and 2017 data-taking, a gradual shift in the timing of the inputs of the ECAL L1 trigger in the region at $|\eta| > 2.0$ caused a specific trigger inefficiency. For events containing an electron (a jet) with p_T larger than $\approx$50 GeV ($\approx$100 GeV), in the region $2.5 < |\eta| < 3.0$ the efficiency loss is $\approx$10–20%, depending on p_T, η, and time. Correction factors were computed from data and applied to the acceptance evaluated by simulation.

5 Event selection

Events in the SR are selected in the eμ, eτ_h, $\mu\tau_h$, and $\tau_h\tau_h$ final states, which account for 94% of the possible final states with a pair of τ leptons. The $\mu\mu$ final state is used to derive the following corrections:

- a correction to the pileup track density in all simulations, described in Section 6.1;
- a correction to the hard scattering track multiplicity in the Drell–Yan and diboson simulations, described in Section 6.2;
- a correction to the elastic photon-induced simulations to include dissociative contributions, described in Section 7;
- a correction to the acoplanarity distribution in the Drell-Yan simulation, described in Section 8.1.

In the eμ final state, events are triggered with a combination of triggers requiring an electron and a muon, with a p_T threshold of 23 GeV for the leading lepton, and 8 or 12 GeV for the subleading lepton if it is a muon or an electron, respectively. Offline, the leading lepton is required to have $p_T > 24\,\mathrm{GeV}$ and the subleading lepton $p_T > 15\,\mathrm{GeV}$. The subleading lepton p_T threshold is several GeV above the trigger p_T thresholds to reduce background processes with misidentified jets. In the eτ_h ($\mu\tau_h$) final states, events are triggered with single electron (muon) triggers with p_T thresholds ranging between 25 and 32 (24 and 27) GeV depending on

Table 1: Baseline selection criteria used in the different final states of the SR and in the $\mu\mu$ CR. The electrons, muons, and τ_h are required to be well identified and isolated. The p_T and pseudorapidity ranges correspond to different sets of triggers, and different data-taking periods.

	$e\mu$	$e\tau_h$	$\mu\tau_h$	$\tau_h\tau_h$	$\mu\mu$
p_T^e (GeV)	$> 15/24$	$> 25 - 33$	—	—	—
$\lvert\eta^e\rvert$	< 2.5	$< 2.1 - 2.5$	—	—	—
p_T^μ (GeV)	$> 24/15$	—	$> 21 - 29$	—	$> 26 - 29/10$
$\lvert\eta^\mu\rvert$	< 2.4	—	$< 2.1 - 2.4$	—	
$p_T^{\tau_h}$ (GeV)	—	$> 30 - 35$	$> 30 - 32$	> 40	—
$\lvert\eta^{\tau_h}\rvert$	—	$< 2.1 - 2.3$	$< 2.1 - 2.3$	< 2.1	—
$m_{\mu\mu}$ (GeV)	—	—	—	—	> 50
OS	yes	yes	yes	yes	yes
$\lvert d_z(\ell, \ell')\rvert$ (cm)	< 0.1	< 0.1	< 0.1	< 0.1	< 0.1
$\Delta R(\ell, \ell')$	> 0.5	> 0.5	> 0.5	> 0.5	> 0.5
$m_T(e/\mu, \vec{p}_T^{\text{miss}})$ (GeV)	—	< 75	< 75	—	—

the data-taking year. Additional events with lepton p_T as low as 24 (19) GeV and $\lvert\eta\rvert < 2.1$ can be selected using cross triggers requiring also the presence of a τ_h candidate with p_T above 20 (27) GeV and $\lvert\eta\rvert < 2.1$. In these two final states, the background from W + jets is reduced by requiring the transverse mass between the lepton and $\vec{p}_T^{\text{miss}}$, $m_T(e/\mu, \vec{p}_T^{\text{miss}})$, to be less than 75 GeV. The events in the $\tau_h\tau_h$ final state are selected with triggers requiring the presence of two loosely isolated τ_h candidates with $p_T > 35 - 40$ GeV and $\lvert\eta\rvert < 2.1$. The offline thesholds are $p_T > 40$ GeV and $\lvert\eta\rvert < 2.1$ for all the data-taking periods. A trigger requiring a single muon with $p_T > 24$–27 GeV is used to select events in the $\mu\mu$ final state. Offline, the leading (subleading) muon is required to have $p_T > 26$—29(10) GeV and $\lvert\eta\rvert < 2.4$. The invariant mass of the two muons, $m_{\mu\mu}$, must be greater than 50 GeV.

In all final states, the two objects are required to be well-identified and isolated, to have opposite sign (OS) charge, to be separated from each other by $\Delta R = \sqrt{(\Delta\eta)^2 + (\Delta\phi)^2} > 0.5$, and to satisfy $\lvert d_z(\ell, \ell')\rvert < 0.1$ cm, where $\lvert d_z(\ell, \ell')\rvert$ is the difference in the longitudinal impact parameters of the two objects. Final states are made mutually exclusive by vetoing events that have additional identified and isolated electrons or muons.

The criteria listed above and summarized in Table 1 constitute the baseline selection, on top of which other requirements can be applied to define the SR or the control regions (CRs) used to derive corrections. In particular, events in the SR are required to have low acoplanarity and track multiplicity, as described in the following paragraphs, in order to improve the signal-to-background ratio using the characteristics of the exclusive process signature.

The acoplanarity, defined as:

$$A = 1 - \lvert\Delta\phi(\ell, \ell')\rvert/\pi, \tag{7}$$

is typically small for photon-induced elastic events, for which the leptons are produced back-to-back. In the case of τ leptons, A is computed using the visible decay products, which are closely aligned with the original τ lepton before decay, especially at high p_T. In the SR, the events are required to have $A < 0.015$. This requirement has a signal efficiency ranging from 95% in the $e\mu$ final state to $> 99\%$ in the $\tau_h\tau_h$ final state.

Elastic signal events are also characterized by a low track multiplicity (N_{tracks}) at the dilepton

vertex. The dilepton vertex position along the z axis is calculated as the average z of the two objects. The variable N_{tracks} is estimated by counting the number of tracks that have a z coordinate within a 0.1 cm wide window centered around the dilepton vertex, removing the tracks that were used to build the lepton candidates. The SRs are defined with $N_{\text{tracks}} = 0$ or 1. About 50 (25)% of the signal events have $N_{\text{tracks}} = 0$ (1). This fraction is larger far from the beamspot position, where the contribution from PU tracks is less important.

The activity in the tracker impacts the identification of electrons, muons, and τ_{h} candidates, typically leading to a higher efficiency. Scale factors are computed to match the simulated efficiencies to the observed efficiencies for objects surrounded by a low track activity at their vertex, after the standard corrections independent of N_{tracks} are applied.

6 Corrections to the simulated track multiplicity

The simulations are corrected to describe well N_{tracks}, the track multiplicity around the dilepton vertex. Corrections for two sources of tracks are derived: tracks originating from the pileup (Section 6.1) and tracks originating from the hard scattering and underlying event activity (Section 6.2). They are derived from CRs in the dimuon final state and applied to simulations in the SRs.

6.1 Tracks originating from the pileup

While the PU multiplicity in simulation is reweighted to match that observed in the data, the PU track density along the z axis in simulation needs to be corrected to better describe N_{tracks} at the dilepton vertex. First, the simulations are corrected such that the beamspot position (z_{BS}) and beamspot width (σ_{BS}) distributions are similar to the observed ones, and the PU tracks are redistributed accordingly along the z axis, as explained below. Simulated events originally all have $\sigma_{\text{BS}} = 3.5\,\text{cm}$, whereas the observed σ_{BS} distribution is spread between about 3.0 and 3.8 cm. Simulated events are assigned randomly corrected beamspot properties, $z_{\text{BS}}^{\text{corr}}$ and $\sigma_{\text{BS}}^{\text{corr}}$, following the corresponding profiles in data. The z position of PU tracks, identified as such if they are not matched to generator-level information, are redistributed along the z axis and assigned a corrected z position:

$$z^{\text{corr}} = z_{\text{BS}}^{\text{corr}} + \frac{\sigma_{\text{BS}}^{\text{corr}}}{\sigma_{\text{BS}}^{\text{sim}}} \left(z - z_{\text{BS}}^{\text{sim}} \right). \tag{8}$$

A residual correction to the PU track density is derived in a $Z \to \mu\mu$ CR, defined with the selection criteria for the $\mu\mu$ final state detailed in Section 5, with the additional requirement that $m_{\mu\mu}$ is within 15 GeV of the true Z boson mass, m_Z. The track multiplicity is counted in data and in simulation in windows of 0.1 cm width along the z axis, for windows centered at least 1 cm away from the reconstructed dimuon vertex, as illustrated in Fig. 2. This last requirement ensures that all tracks in the windows come from PU and not from the hard scattering interaction. Weights are derived as functions of the PU track multiplicity and window z position so as to match the N_{tracks} distribution in data. Distributions of the number of PU tracks, $N_{\text{tracks}}^{\text{PU}}$, are shown in data, uncorrected, and beamspot-corrected simulations in Fig. 3, for windows with different z positions. About one third of the windows situated at the beamspot center do not have any PU track. This fraction reaches about one half (80%) one (two) beamspot widths away from the beamspot center. The correction to the simulated event weight is in the range 0.89–1.00 (0.93-1.16) for $N_{\text{tracks}}^{\text{PU}} = 0$ ($N_{\text{tracks}}^{\text{PU}} = 1$) over the whole z axis and data-taking periods.
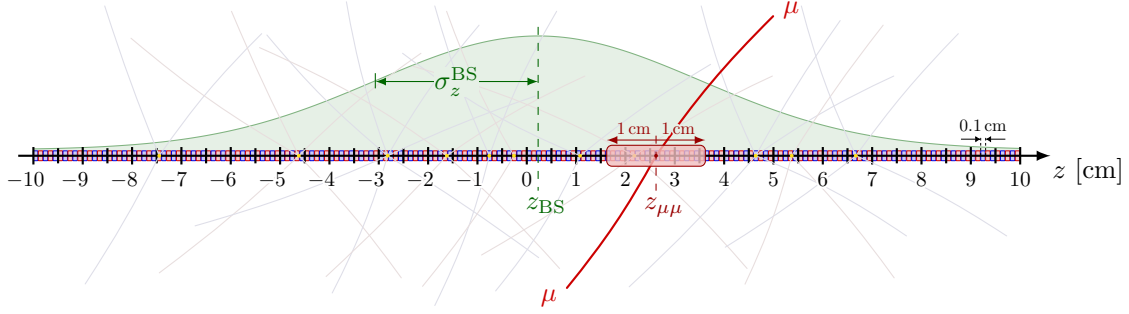
Figure 2: Schematic view of the 0.1 cm-wide windows probed along the z axis to derive corrections to the PU track density in simulation. Windows within 1 cm from the dimuon vertex, illustrated with the red box, are discarded so as not to count tracks from the hard scattering interaction. The green curve indicates the position and width of the beamspot.
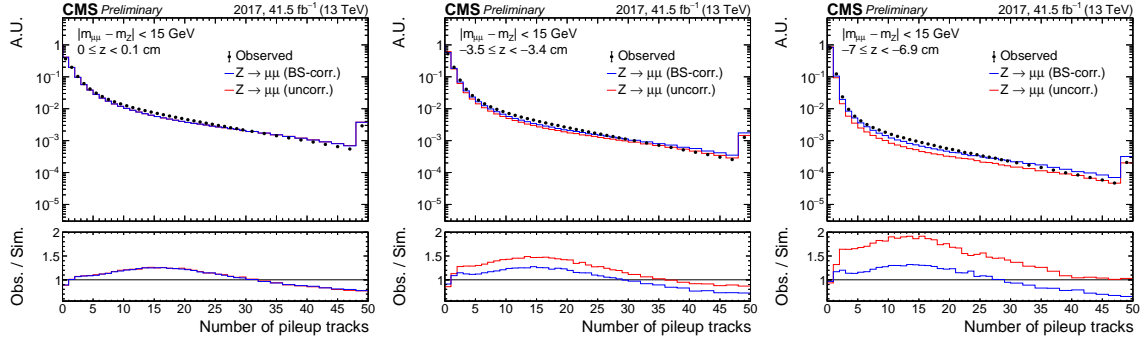

Figure 3: Distribution of $N_{\text{tracks}}^{\text{PU}}$ in windows of 0.1 cm width along the z axis in data (black), uncorrected simulation (red), and beamspot-corrected simulation (blue) in data collected in 2017. The windows shown here are located at the beamspot center (left), and one (center) or two (right) beamspot widths away from the center. The ratio of corrected simulation to data is taken as a correction to the simulations.

6.2 Tracks originating from the hard scattering and underlying event activity

The only major background in the SR estimated using simulation is the Drell–Yan production of a lepton pair. The number of tracks coming from the hard scattering interaction is not well described in the simulation, and corrections are derived from the same $Z \rightarrow \mu\mu$ CR. To derive this correction, the number of tracks around the reconstructed dimuon vertex is compared between data and simulation.

As shown in Fig. 4, the simulation is split into several components depending on the number of tracks originating from the hard scattering interaction, as determined from generator-level information, and reconstructed with $p_{\text{T}} > 0.5$ GeV and $|\eta| < 2.5$. The total number of reconstructed tracks is the sum of these tracks and those associated with PU interactions: $N_{\text{tracks}} = N_{\text{tracks}}^{\text{HS}} + N_{\text{tracks}}^{\text{PU}}$. Events from the exclusive photon-induced production of a pair of muons or W bosons, which contribute only significantly at low N_{tracks}, are estimated from simulation and subtracted.

The PU track density is first corrected with the weights described in Section 6.1, while the reweighting factors for each Drell–Yan component with a given number of $N_{\text{tracks}}^{\text{HS}}$ is determined iteratively by matching the simulation to the data, starting from events with $N_{\text{tracks}} = 0$, to which only the simulated component with $N_{\text{tracks}}^{\text{HS}} = 0$ contributes. The event weight correction is as low as 0.61 ± 0.04 (0.76 ± 0.04) for $N_{\text{tracks}}^{\text{HS}} = 0$ ($N_{\text{tracks}}^{\text{HS}} = 1$). This correction is also applied

to the minor diboson production background with 2 leptons and 2 neutrinos in the final state, which has the same generator settings.
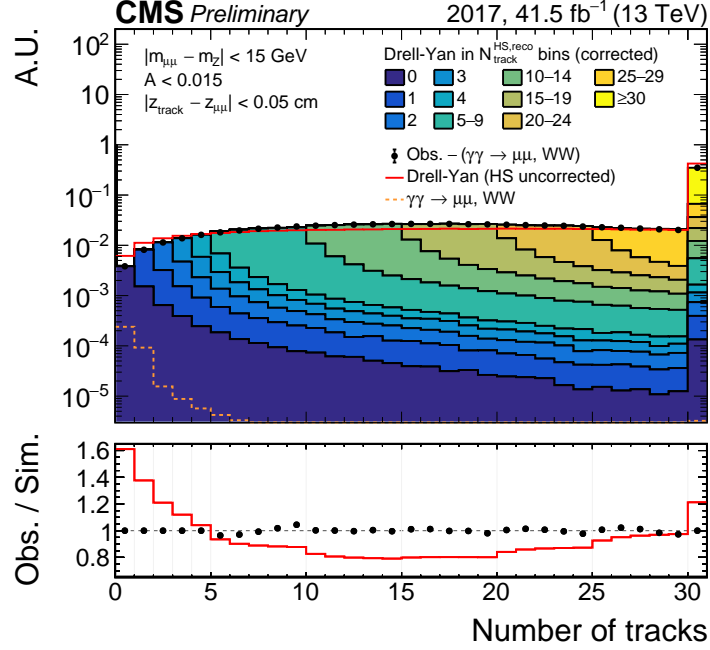

Figure 4: Distribution of the number of reconstructed tracks in a 0.1 cm-wide window in the z direction, centered on the dimuon reconstructed vertex, for $A < 0.015$. The Drell–Yan simulation is split into several components based on the number of reconstructed tracks originating from the hard interaction. The red line shows the simulation before the correction. The expected contribution from the $\gamma\gamma \rightarrow \mu\mu$ and $\gamma\gamma \rightarrow WW$ processes (dashed orange line) has been subtracted from observed data. The last bin includes the overflow.

7 Signal estimation

The signal is modelled using simulated elastic events. The semi-dissociative and fully dissociative production modes are much less likely to satisfy the acoplanarity and N_{tracks} requirement but their cross sections are larger, such that they are not negligible in the SR. The elastic prediction is rescaled to account for the semi-dissociative and fully dissociative contributions as explained in the next paragraph.

The scaling factor is measured in data in a $\mu\mu$ CR, defined with the baseline selection and $N_{\text{tracks}} = 0$ or 1 and $A < 0.015$ as additional requirements. In that CR, shown in Fig. 5, the inclusive backgrounds, dominated by the Drell–Yan production of a muon pair, are estimated together from data. Their $m_{\mu\mu}$ distribution is taken from observed events with $3 < N_{\text{tracks}} < 7$. These thresholds ensure that the photon-induced contributions are negligible while the N_{tracks} selection is close enough to that in the SR to have an unbiased $m_{\mu\mu}$ distribution. The $m_{\mu\mu}$ distribution is reweighted so that the inclusive background normalization in the range $|m_{\mu\mu} - m_Z| < 15\,\text{GeV}$ matches the data count in the same range. The elastic $\gamma\gamma \rightarrow \mu\mu$ process is then rescaled to match the difference between the data and the inclusive backgrounds away from the Z peak region.

Assuming there is no dependence on the dilepton mass, $m_{\ell\ell}$, the scaling factor to include the dissociative contributions is 2.70 ± 0.04 (2.71 ± 0.10) for $N_{\text{tracks}} = 0$ (1), where the uncertainty is statistical only. This is compatible with the value predicted by the SUPERCHIC generator, using
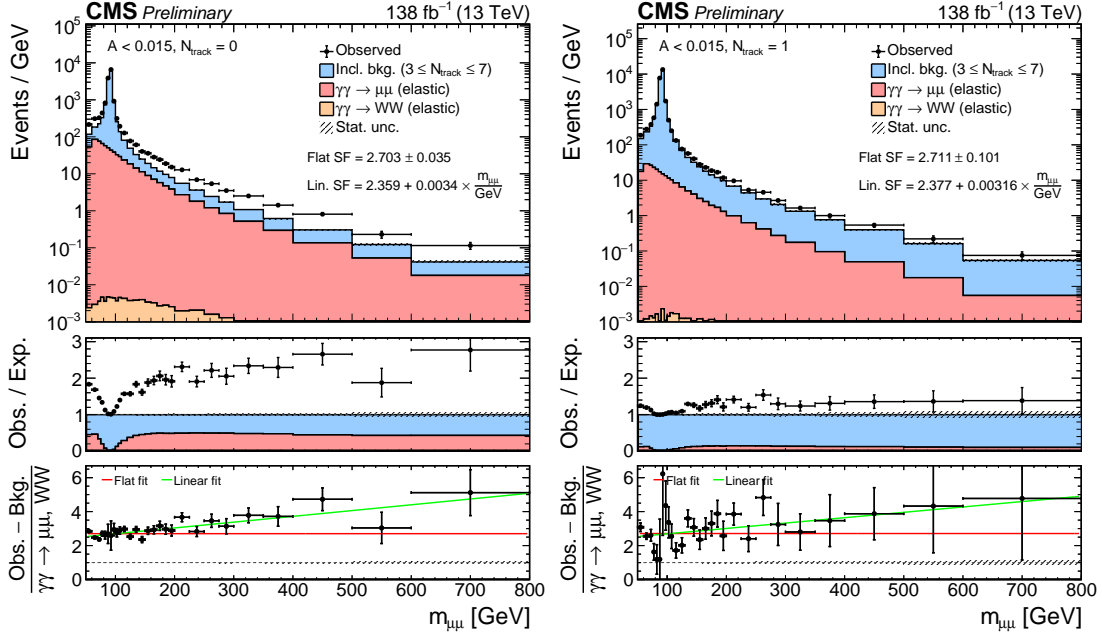
Figure 5: Measurement of the scaling factor for the elastic-elastic exclusive signal in $\mu\mu$ events for $N_{\text{tracks}} = 0$ (left) or 1 (right), and $A < 0.015$. The shape of the inclusive background (blue) is estimated from the observed data in the $3 \leq N_{\text{tracks}} \leq 7$ sideband, and rescaled to fit the observed data in $75 < m_{\mu\mu} < 105\,\text{GeV}$. The scaling factor is fitted in the bottom ratio pad with constant (red) and linear (green) functions.

the same acoplanarity requirement $A < 0.015$. The scaling factor is also fitted as a linear function of $m_{\mu\mu}$ and, in that case, is equal to $2.359 + 0.0034\,m_{\mu\mu}/\text{GeV}$ ($2.377 + 0.00316\,m_{\mu\mu}/\text{GeV}$) for $N_{\text{tracks}} = 0$ (1). A linear dependency of the scaling factor with $m_{\ell\ell}$ is assumed as a nominal correction in the SRs, whereas the flat value is considered as a systematic uncertainty as detailed in Section 9. Elastic events in the SR, coming from the $\gamma\gamma \to \tau\tau/\text{ee}/\mu\mu/\text{WW}$ simulations, are all rescaled with this correction as a function of the dilepton or diboson mass, to include semi-dissociative and fully-dissociative contributions.

8 Background estimation

In the SR, the dominant backgrounds are the Drell–Yan production of a lepton pair and processes with a jet misidentified as an electron, a muon, or a τ_{h} candidate, collectively denoted as "jet mis-ID background". The jet mis-ID background is essentially composed of W + jets and QCD multijet events. The photon-induced production of a pair of W bosons is reduced with the acoplanarity requirement, and is significant only in the eμ final state, where its expected normalization is about 4% of that of the exclusive di-τ production. The photon-induced production of an electron (muon) pair is about 50 (4)% of the signal expected contribution in the eτ_{h} ($\mu\tau_{\text{h}}$) final state. When there is no exclusivity requirement relying on A nor N_{tracks}, the t$\bar{\text{t}}$, inclusive diboson, and single-top-quark processes also contribute.

8.1 Drell–Yan

The Drell–Yan process is estimated using simulation. The corrections described in Section 6 are applied to improve the description of $N_{\text{tracks}}^{\text{PU}}$ and $N_{\text{tracks}}^{\text{HS}}$. The acoplanarity is observed to be mismodeled in simulation in a $\mu\mu$ CR, defined with the selection criteria from Section 5 and further enriched in Drell–Yan events by requiring $|m_{\mu\mu} - m_{\text{Z}}| < 15\,\text{GeV}$. An acoplanarity

correction, measured in two-dimensional bins of the p_T of both muons, is derived in this CR by matching the simulation to the observed data. This correction is applied to simulated Drell–Yan events in the SR on the basis of the generated τ lepton p_T before their decays.

The simulation size is limited, and large statistical uncertainties arise when requiring $N_{\text{tracks}} = 0$ or 1. To reduce this effect, the Drell-Yan contribution in the SR is estimated from simulated events with $N_{\text{tracks}} < 10$, which constitute about 10% of the total number of Drell-Yan events. The upper bound ensures a similar event topology as in the SR, allowing the $m_{\tau\tau}$ distributions to be similar. The distribution derived with $N_{\text{tracks}} < 10$ is scaled to predict the Drell–Yan events with $N_{\text{tracks}} = 0$ or 1. The scaling factors are derived in the eμ final state with a large simulation of $Z \rightarrow \tau\tau$ events with only leptonic τ decays. They are equal to $2.48 \pm 0.05\%$ and $5.10 \pm 0.07\%$, for $N_{\text{tracks}} = 0$ and 1, respectively.

8.2 Backgrounds with misidentified jets in the $e\tau_h$ and $\mu\tau_h$ final states

The mis-ID background with a jet misidentified as a τ_h candidate is estimated from data. In the $e\tau_h$ and $\mu\tau_h$ final states, the dominant processes contributing to the mis-ID background are W + jets and QCD multijet events. The jet misidentification factors (MFs) depend on the process because of different topologies and jet flavors, and they are therefore measured in two different CRs. A CR enriched in W + jets events is built by requiring $m_T > 75\,\text{GeV}$, while a QCD-enriched CR is obtained by requiring the two objects to have same-sign (SS) charge. In these CRs, the MFs are measured for each data-taking period, separately for each τ_h DM, by taking the ratio of events in which the τ_h candidate passes the SR τ_h identification criteria, to events in which the τ_h candidate fails these criteria but passes looser ones. Events where the τ_h candidate is genuine or corresponds to a misidentified electron or muon are evaluated using simulation and subtracted from the CR. The MFs are fitted as a function of the τ_h p_T and range from about 0.03 for the $h^{\pm}h^{\mp}h^{\pm} + \pi^0(s)$ DM, to about 0.40 for the $h^{\pm}$ DM. These MFs are multiplied by a factor of about 1.7 when the events are selected with cross-triggers relying on the presence of a τ_h candidate because of the isolation cuts applied at trigger level.

The track activity around the di-τ impacts the calculation of the τ_h isolation, which enters the τ_h identification discriminator, such that the MFs are expected to depend on N_{tracks}. For each τ_h DM, the MFs determined for given ranges of N_{tracks} are divided by the average MF measured inclusively in N_{tracks} to obtain a multiplicative N_{tracks}-dependent correction, $\omega(N_{\text{tracks}}, \text{DM}^{\tau_h})$, to the p_T- and decay-mode-dependent MFs determined previously. The corrected MFs can then be written, for each CR, as:

$$\text{MF}^{\text{corr}}(p_T^{\tau_h}, \text{DM}^{\tau_h}, N_{\text{tracks}}) = \text{MF}(p_T^{\tau_h}, \text{DM}^{\tau_h})\omega(N_{\text{tracks}}, \text{DM}_h^{\tau}). \qquad (9)$$

The $\omega(N_{\text{tracks}}, \text{DM}^{\tau_h})$ corrections are measured for the combination of the different data-taking years. Because statistical uncertainties are large at low N_{tracks}, $\omega(N_{\text{tracks}}, \text{DM}_h^{\tau})$ is fitted with an exponential function for $N_{\text{tracks}} < 10\text{–}15$, as shown in Fig. 6 for the $h^{\pm} + \pi^0(s)$ DM in the $e\tau_h$ final state.

The total MF, MF_{tot}, is computed as a weighted average of the MFs determined in the high-m_T and SS CRs, according to the expected relative fraction of W + jets and QCD multijet events:

$$\text{MF}_{\text{tot}} = x^{\text{QCD}}\text{MF}_{\text{SS}}^{\text{corr}} + (1 - x^{\text{QCD}})\text{MF}_{\text{high-}m_T}^{\text{corr}}, \qquad (10)$$

where $x^{\text{QCD}} = N^{\text{QCD}}/(N^{\text{QCD}} + N^{\text{W}})$. The number of W + jets events passing the baseline selection, N^{W}, is determined from simulations, while the same quantity for QCD multijet events, N^{QCD}, is taken as the difference between data and simulated predictions for other processes in the SS CR.
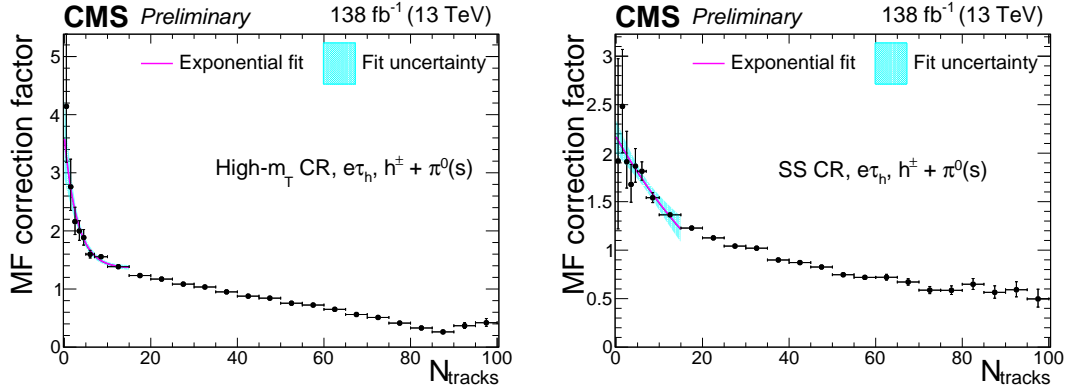
Figure 6: Multiplicative N_{tracks}-dependent corrections to the τ_h MFs, $\omega(N_{\text{tracks}}, \text{DM}_h^\tau)$, in the $e\tau_h$ final state, in the high-m_T (left) and SS (right) CRs, for the $h^\pm + \pi^0$(s) DM. The cyan shaded area corresponds to the fit uncertainty.

To estimate the mis-ID background in the SR in the $e\tau_h$ and $\mu\tau_h$ final states, events passing the SR selection with the exception that the τ_h candidate fails the τ_h nominal identification but passes looser criteria, are reweighted with MF_{tot}. Contributions from events with real τ_h, electrons, or muons are estimated from simulation and subtracted from the anti-isolated region.

8.3 Backgrounds with misidentified jets in the $\tau_h\tau_h$ final state

In the $\tau_h\tau_h$ final state, the mis-ID background is mostly composed of QCD multijet events and the MFs are determined in a single CR where the τ_h candidates have SS charge. The MFs for the leading (subleading) τ_h are measured in events in which the subleading (leading) τ_h passes or fails the tight identification criteria. They are in the range 0.05–0.38 depending on the τ_h DM.

The N_{tracks}-dependent correction is derived in a similar way as in the $e\tau_h$ and $\mu\tau_h$ final states, and is between 1.8 and 2.3 for events with $N_{\text{tracks}} = 0$. In this final state, the number of events selected at low N_{tracks} is larger because of the inversion of the isolation of both τ_h candidates, and contributions from exclusive dijet production become significant in the lowest N_{tracks} bins, such that no fit is performed to the $\omega(N_{\text{tracks}}, \text{DM}_h^\tau)$ distributions, and the values measured for $N_{\text{tracks}} = 0, 1$ are used without constraints from higher N_{tracks} bins.

In the SR, events where the leading (subleading) τ_h is a misidentified jet are estimated by scaling with the MFs events where the leading (subleading) τ_h is anti-isolated and the subleading (leading) τ_h is isolated. These contributions both include events where both the leading and subleading τ_h candidates are misidentified jets. To remove the double counting, events with two misidentified jets are estimated by scaling events where the two τ_h candidates are anti-isolated with the product of the MFs for each object, and are subtracted.

8.4 Backgrounds with misidentified jets in the $e\mu$ final state

In the $e\mu$ final state, the mis-ID background with a jet misidentified as an electron or a muon, essentially composed of W + jets and QCD multijet events, is estimated from events where the electron and muon have SS charge. Events passing the SR selection with the exception that the electron and muon have SS charge are reweighted with a two-dimensional scaling factor dependent on the electron and muon p_T. This factor is measured by taking the ratio of OS to SS events where the muon isolation is inverted, subtracting non-jet contributions estimated from simulation. It is in the range 1.4–2.1 depending on the lepton p_T.

A bias is introduced by the inversion of the muon isolation, and a correction to the scaling factor

is measured by taking the ratio of the scaling factors measured in events where the electron identification is inverted, and the muon isolation is inverted or not. The correction ranges between 1.0 and 2.7 depending on the lepton p_T.

A multiplicative correction for the dependency of the scaling factor with N_{tracks} is measured by fitting the ratio of the scaling factors in exclusive ranges of N_{tracks} over the average inclusive scaling factor. At $N_{\text{tracks}} = 0$, the correction is about 0.89 ± 0.07.

While the normalization of the jet mis-ID background is estimated with the procedure described above, its m_{vis} distribution is taken from SS data events with $N_{\text{tracks}} < 10$, from which backgrounds other than the jet mis-ID component are subtracted using their simulated expectations. This method reduces statistical fluctuations in the m_{vis} templates.

8.5   Other backgrounds

Minor contributions from diboson events to the SR, mostly WW events, are estimated from simulation. The exclusive $\gamma\gamma \to \text{WW}$, $\gamma\gamma \to \text{ee}$, and $\gamma\gamma \to \mu\mu$ events, which contribute mostly to the $\text{e}\mu$, $\text{e}\tau_h$, and $\mu\tau_h$ final states, respectively, are estimated from the elastic simulation and rescaled with the same correction as the signal samples to include the dissociative components.

The agreement between data and predictions is checked in events passing the selection without the N_{tracks} and acoplanarity requirements. The single-top quark, $\text{t}\bar{\text{t}}$, and Higgs boson processes, which do not contribute to the SR with $N_{\text{tracks}} < 2$, are included using their prediction from simulation. The agreement is good for all final states.

9   Systematic uncertainties

Systematic uncertainties are considered as nuisance parameters in the statistical procedure to extract the signal significance, its signal strength μ, and constraints on a_τ and d_τ. The signal strength μ is defined as the ratio between the observed cross section of the $\gamma\gamma \to \tau\tau$ process to the theoretical cross section predicted by the GAMMA-UPC generator for the elastic component corrected by the multiplicative experimental scaling to include dissociative contributions.

The integrated luminosities for the 2016, 2017, and 2018 data-taking years have 1.2–2.5% individual uncertainties [56–58], while the overall uncertainty for the 2016–2018 period is 1.6%. The uncertainty in the Drell–Yan theoretical cross section is 2%.

The uncertainties in the muon and electron identification, isolation, and triggering efficiencies are up to 2% per object. Uncertainties related to the τ_h trigger efficiency depend on DM^{τ_h} and are up to 5%. Several uncertainties, stemming from statistical and systematic sources in the measurement, affect the τ_h identification, with different correlations across data-taking years and various dependencies on the τ_h DM and its p_T. This uncertainty is up to 5% in the p_T range considered in this analysis, and propagates directly to the measured signal strength. Electrons (muons) misidentified as τ_h candidates, coming mostly from the $\text{Z} \to \text{ee}$ ($\text{Z} \to \mu\mu$) process, have normalization uncertainties of the order of 10 (10)%. The uncertainty in the τ_h energy scale is up to 1.2%, whereas electrons (muons) misidentified as τ_h have energy scale uncertainties up to 5 (1)%. Multiplicative corrections to the scale factors to account for the low N_{tracks} environment have uncertainties of 2.1, 2.0, 15, and 22% for genuine τ_h candidates, electrons, muons misidentified as τ_h candidates, and electrons misidentified as τ_h candidates, respectively.

The uncertainty in the $N_{\text{tracks}}^{\text{PU}}$ correction amounts to 2%, which covers the effects of the beamspot

width and position correction. The uncertainty in the $N_{\text{tracks}}^{\text{HS}}$ correction is taken to have the same magnitude as the relative fraction of $\gamma\gamma \to \mu\mu/WW$ events in the CR where the correction is derived, and it amounts to 6.5 (1.5)% in the $N_{\text{tracks}} = 0(1)$ category. The statistical uncertainty in the correction is negligible with respect to this systematic component. This uncertainty contributes a 7% effect in the measured signal strength as shown in Fig. 7 (second line) and is among the leading systematic uncertainties in this analysis.

The correction to the acoplanarity distribution in simulated Drell–Yan events leads to a 5% normalization uncertainty, arising from the finite granularity used to bin the correction as a function of the p_{T} of the two leptons. An uncertainty of 2.0 (1.4)% is associated with the estimation of the Drell–Yan events in the SR with $N_{\text{tracks}} = 0(1)$ from simulated events with $N_{\text{tracks}} < 10$. Uncertainties arising from the renormalization and factorization scales, as well as from the PDF set, are also taken into account for the Drell–Yan simulation, after propagation to the acoplanarity correction.

The uncertainty in the predictions of the jet mis-ID background in final states with τ_{h} candidates comes from several sources:

- A statistical uncertainty in the inclusive MFs, growing linearly to 50% for $p_{\text{T}}^{\tau_{\text{h}}} = 300\,\text{GeV}$, independently for each DM and data-taking year;
- A statistical uncertainty in the N_{tracks} correction, amounting to 18 (16, 6)% in the $e\tau_{\text{h}}$ ($\mu\tau_{\text{h}}$, $\tau_{\text{h}}\tau_{\text{h}}$) SRs;
- A systematic uncertainty in the inclusive MFs, coming from the inversion of selection requirements to define the CRs, reaching up to 10%;
- A systematic uncertainty in the calculation of the relative fraction of W + jets and QCD multijet events in the $e\tau_{\text{h}}$ and $\mu\tau_{\text{h}}$ SRs, leading to a 9% normalization effect;
- A systematic uncertainty in the N_{tracks} correction, arising from the choice of the fit function and fit range, with an effect up to 10% for $N_{\text{tracks}} = 0$.

Statistical uncertainties in the OS-to-SS scaling factor used to evaluate the mis-ID background in the $e\mu$ final state are included, independently for each bin in electron and muon p_{T} where the measurement is performed. A systematic uncertainty of 10% is considered on top to cover for a potential difference in the background composition in the SR and CR. The extrapolation of the scaling factor to $N_{\text{tracks}} = 0$ has a total uncertainty of 8%, arising from the choice of the fit function and from the limited number of events in the measurement.

Most theoretical and experimental uncertainties cancel when renormalizing the signal prediction using the scaling factor derived from the $\mu\mu$ CR for the $\gamma\gamma \to \mu\mu$ process. The uncertainty in the scaling factor is composed of a normalization component from statistical origin, amounting to 1.3 (3.7)% for $N_{\text{tracks}} = 0$ (1), and a component with a shape dependence on $m_{\tau\tau}$. The latter component consists in considering as a 1 s.d. effect the possibility that the scaling factor does not depend on $m_{\ell\ell}$, and is symmetrized with respect to the nominal hypothesis of a linear dependence with $m_{\ell\ell}$. This $m_{\tau\tau}$-dependent uncertainty is the leading uncertainty in the measurement of the $\gamma\gamma \to \tau\tau$ process, as shown in Fig. 7 (first line), and contributes a 16% uncertainty to the measured signal strength. These uncertainties are also considered for the photon-induced WW, ee, and $\mu\mu$ productions.

Statistical uncertainties in the number of simulated background events in the SR or observed event yields in the CRs used to derive the jet mis-ID background are considered in all bins of the distributions using the approach from Ref. [59]. The systematic uncertainty in the pileup modelling is taken into account by varying by $\pm 4.6\%$ the total inelastic cross section used to
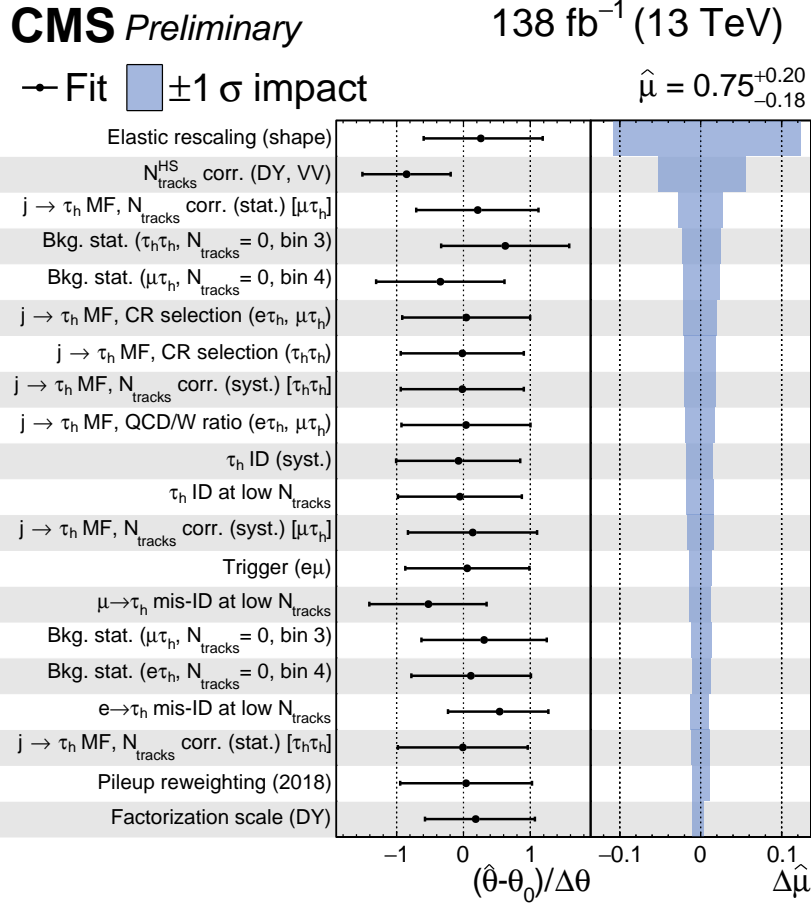
Figure 7: Postfit values of the nuisance parameters (black markers), shown as the difference of their best-fit values, $\hat{\theta}$, and prefit values, θ_0, relative to the prefit uncertainties $\Delta\theta$. The impact $\Delta\hat{\mu}$ of the nuisance parameters on the signal strength is computed as the difference of the nominal best fit value of μ and the best fit value obtained when fixing the nuisance parameter under scrutiny to its best fit value $\hat{\theta}$ plus/minus its postfit uncertainty (blue shaded area). The nuisance parameters are ordered by their impact, and only the 20 highest ranked parameters are shown.

calculate simulated pileup distributions [60].

The impacts of the leading systematic uncertainties in the measurement of the signal strength, which is described in Section 10.1, are shown in Fig. 7.

10 Results

The significance of the photon-induced $\gamma\gamma \to \tau\tau$ process, as well as the constraints on a_τ and d_τ, are extracted from the m_{vis} distributions in the four final states and in the two N_{tracks} bins, shown in Figs. 8–9. The last bins include events up to $m_{\text{vis}} = 500\,\text{GeV}$, while events at higher m_{vis} are discarded to ensure a sufficient difference with the Λ scale used in the BSM interpretation. This upper threshold removes SM signal events at the percent level. The systematic uncertainties described in Section 9 are included in the statistical procedure as nuisance parameters. The number of data events in the $N_{\text{tracks}} = 0$ SRs, with the additional requirement that m_{vis} is greater than $100\,\text{GeV}$ to reduce the Drell–Yan background contribution, is compared
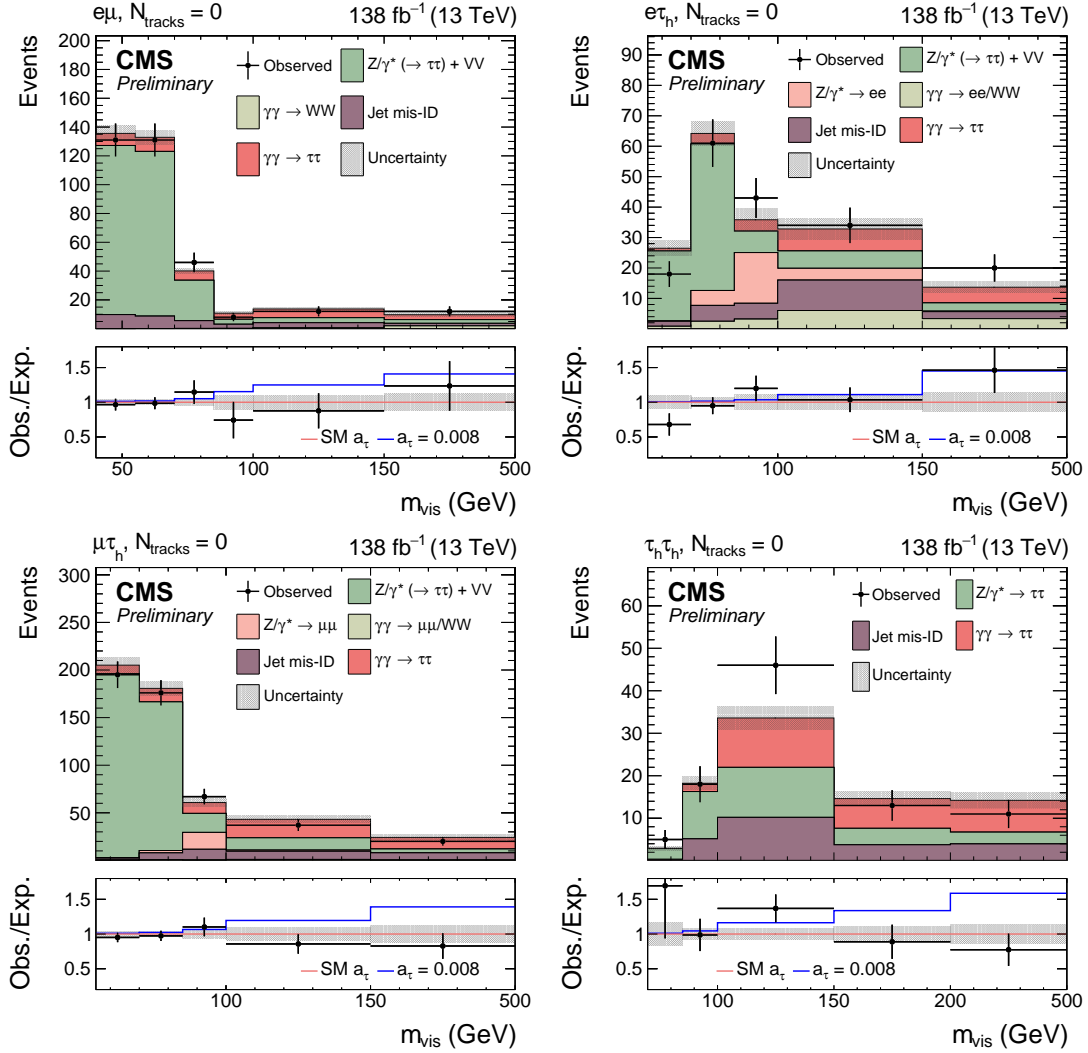
Figure 8: Observed and predicted m_{vis} distributions in the $e\mu$ (upper left), $e\tau_{\text{h}}$ (upper right), $\mu\tau_{\text{h}}$ (lower left), and $\tau_{\text{h}}\tau_{\text{h}}$ (lower right) final states for events with $N_{\text{tracks}} = 0$. The minor inclusive diboson background contribution is drawn together with the Drell–Yan background in the $e\mu$, $e\tau_{\text{h}}$, and $\mu\tau_{\text{h}}$ final states. The normalization of the predicted background distributions corresponds to the result of the global fit. The signal distribution is normalized to its best fit signal strength. The uncertainty band accounts for all sources of background and signal uncertainty, systematic as well as statistical, after the global fit. In the fit, a_τ and d_τ are fixed to their SM values. The ratio of the total predictions for an illustrative value of $a_\tau = 0.008$ to those with SM electromagnetic couplings is shown with a blue line in the bottom panel.

in Table 2 to the background and signal yields in the different final states.

10.1 Observation of $\gamma\gamma \to \tau\tau$

The observed (expected) significance is 5.3 (6.5) s.d. for the exclusive $\gamma\gamma \to \tau\tau$ process. This constitutes the first observation of this process in pp collisions. The corresponding significances per final state are 2.3, 3.0, 2.1, and 3.4 (3.2, 2.1, 3.9, and 3.9) s.d. in the $e\mu$, $e\tau_{\text{h}}$, $\mu\tau_{\text{h}}$, and $\tau_{\text{h}}\tau_{\text{h}}$ final states, respectively. The most sensitive channel in terms of expected significance is $\mu\tau_{\text{h}}$ because of its larger branching fraction with respect to the $e\mu$ final state, its lower p_{T} thresholds and higher lepton efficiencies with respect to the $e\tau_{\text{h}}$ final state, and its lower background
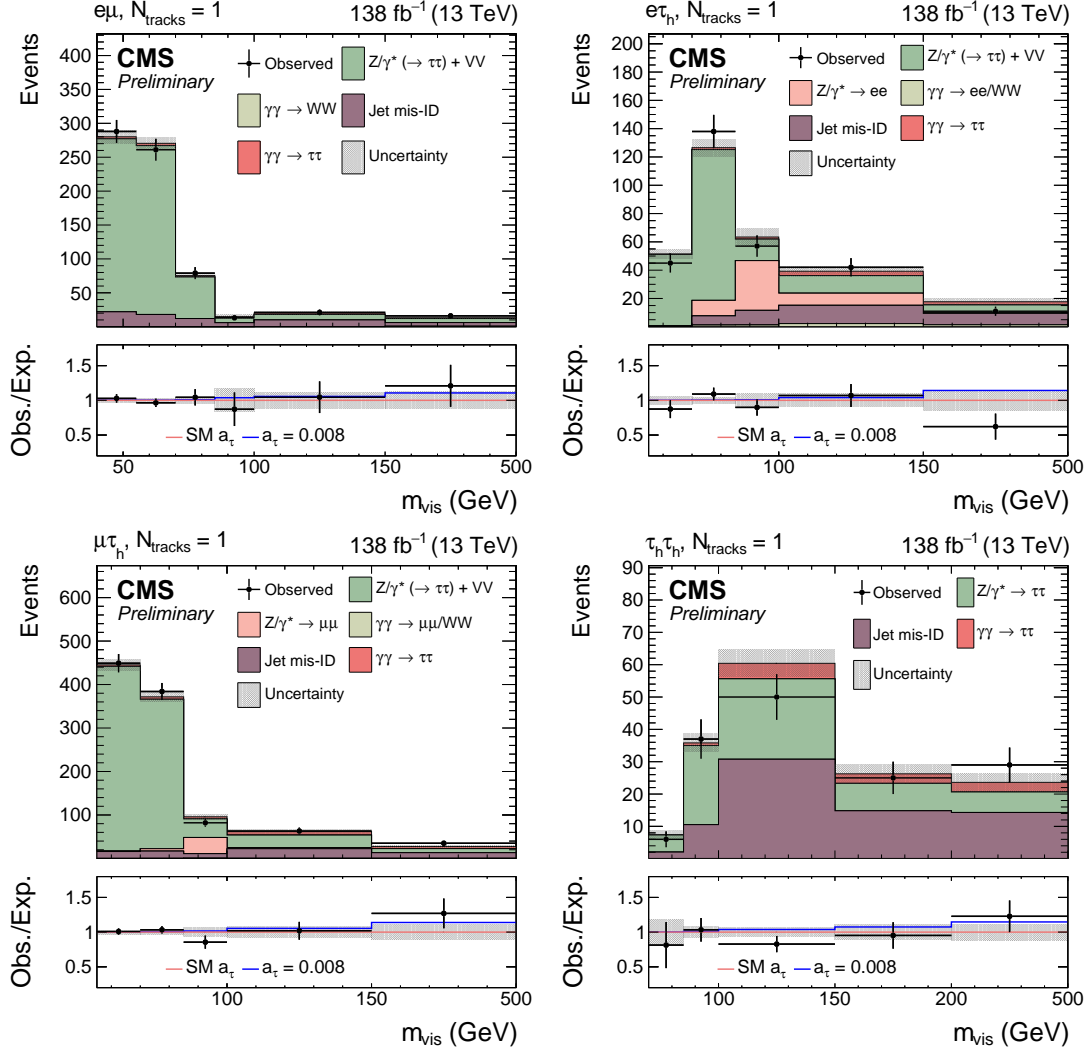
Figure 9: Observed and predicted m_{vis} distributions in the $e\mu$ (upper left), $e\tau_h$ (upper right), $\mu\tau_h$ (lower left), and $\tau_h\tau_h$ (lower right) final states for events with $N_{tracks} = 1$. The description of the histograms is the same as in Fig. 8.

Table 2: Observed and predicted event yields per final state in the signal-enriched phase space with $m_{vis} > 100\,\text{GeV}$ and $N_{tracks} = 0$. The signal and background yields are the result of the global fit including all sources of uncertainties.

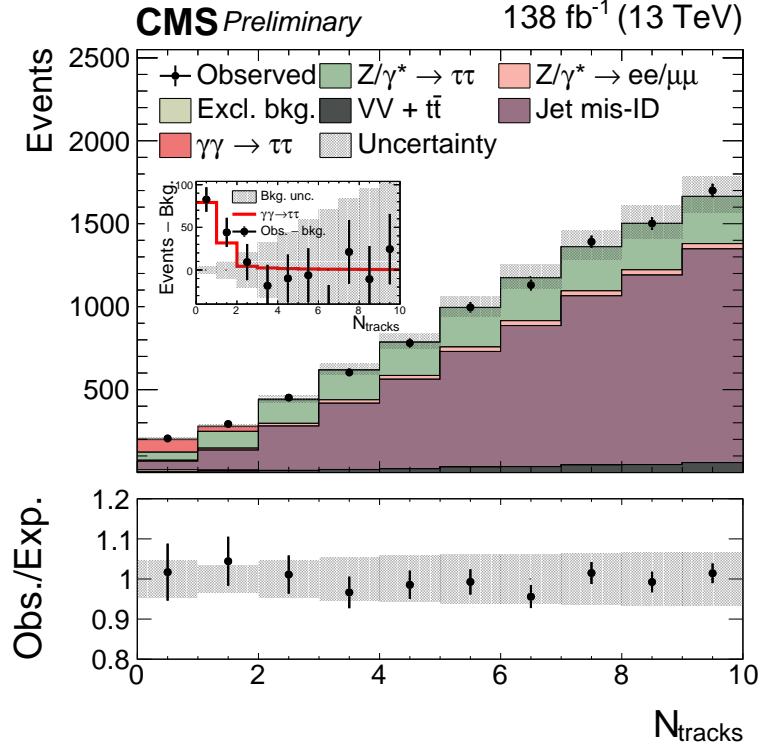| Process	$e\mu$	$e\tau_h$	$\mu\tau_h$	$\tau_h\tau_h$
$Z/\gamma^* \to \tau\tau$	3.6 ± 0.5	9.0 ± 1.2	18.7 ± 2.9	20.2 ± 3.1
$Z/\gamma^* \to ee/\mu\mu$	—	3.9 ± 1.2	1.6 ± 0.6	—
Jet mis-ID	5.0 ± 0.8	11.4 ± 2.9	16.5 ± 3.6	17.5 ± 2.8
Inclusive VV	3.0 ± 0.3	0.2 ± 0.0	0.4 ± 0.0	—
$\gamma\gamma \to ee/\mu\mu$	—	8.1 ± 2.3	1.4 ± 0.2	—
$\gamma\gamma \to WW$	2.5 ± 0.6	0.1 ± 0.0	0.4 ± 0.1	—
Total bkg.	14.1 ± 1.3	32.8 ± 4.8	38.9 ± 4.4	37.7 ± 4.2
Signal	11.9 ± 4.2	15.8 ± 5.7	40.3 ± 14.2	33.4 ± 11.2
Total	26.0 ± 3.8	48.5 ± 4.7	79.2 ± 13.6	71.1 ± 9.3
Observed	24	54	57	70

Figure 10: Observed and predicted N_{tracks} distributions for events passing the SR selection but with the relaxed requirement $N_{\text{tracks}} < 10$ and the additional requirement $m_{\text{vis}} > 100\,\text{GeV}$, combining the $e\mu$, $e\tau_{\text{h}}$, $\mu\tau_{\text{h}}$, and $\tau_{\text{h}}\tau_{\text{h}}$ final states together. The inclusive diboson background contribution is drawn together with the $t\bar{t}$ process. The predicted distributions are adjusted to the result of the global fit performed with the m_{vis} distributions in the SRs, and the signal distribution is normalized to its best fit signal strength. The inset shows the difference between the observed events and the backgrounds, as well as the signal contribution. Systematic uncertainties are assumed to be uncorrelated between final states to draw the uncertainty band.

contributions with respect to the $\tau_{\text{h}}\tau_{\text{h}}$ final state.

The N_{tracks} distribution for events with $N_{\text{tracks}} < 10$ is shown for the combination of final states in Fig. 10 for events with $A < 0.015$, as in the SR, and $m_{\text{vis}} > 100\,\text{GeV}$, so as to reduce the Drell–Yan background contribution. The signal contribution is visible as an excess of events over the inclusive background in the first bins, while the agreement between prediction and observation in the other bins demonstrates a good control of the background modelling and more specifically of the N_{tracks} corrections to the simulations and to the MFs used to predict the background with misidentified jets.

We measure a best-fit signal strength of $\hat{\mu} = 0.75^{+0.21}_{-0.18}$, where the systematic uncertainty dominates over the statistical uncertainty ($\hat{\mu} = 0.75^{+0.17}_{-0.14}\,(\text{syst}) \pm 0.11\,(\text{stat})$). Using only the SRs with $N_{\text{tracks}} = 0$ and discarding the SRs with $N_{\text{tracks}} = 1$, the signal strength becomes $\hat{\mu}(N_{\text{tracks}} = 0) = 0.69^{+0.23}_{-0.19}$.

10.2 Constraints on the anomalous electromagnetic moments of the τ lepton

Constraints on a_τ and d_τ are set independently by performing a negative log-likelihood scan with a_τ and d_τ as single parameters of interest. The SM normalization of $\gamma\gamma \to \tau\tau$ is con-
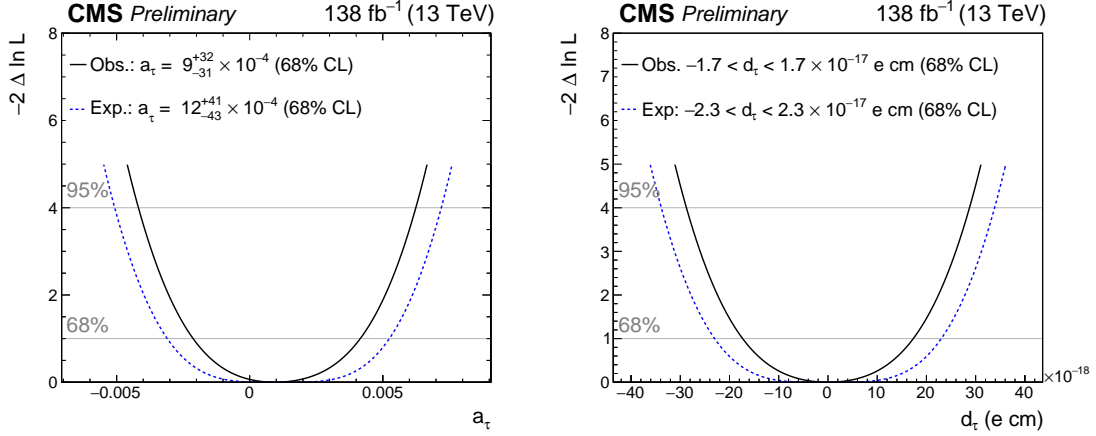
Figure 11: Expected and observed negative log-likelihood scans as a function of a_τ (left) and d_τ (right), for the combination of all SRs in all data-taking periods.

strained to its predicted value [27], estimated from the elastic simulation and weighted with the scaling factor from the $\mu\mu$ CR to include dissociative contributions. Varying a_τ and d_τ from their SM values modifies both the normalization of the signal process and its m_{vis} distribution. In particular, the number of predicted signal events increases with m_{vis} for large $|a_\tau|$ values, as shown in the ratio panels of Figs. 8–9 for an illustrative value of $a_\tau = 0.008$.

The combination of all final states and years gives an observed (expected) best-fit value of $a_\tau = 0.0009^{+0.0032}_{-0.0031}$ $(0.0012^{+0.0041}_{-0.0043})$ at 68% confidence level (CL), as shown in Fig. 11 (left). Contrary to the signal strength measurement assuming SM values for a_τ and d_τ, the statistical uncertainty dominates in the measurement of a_τ because the sensitivity is driven by the high-m_{vis} bins where BSM effects are enhanced: $a_\tau = 0.0009^{+0.0016}_{-0.0015}$ (syst)$^{+0.0028}_{-0.0027}$ (stat). If the measurement was performed using only information about the m_{vis} distribution and with a floating normalization for the $\gamma\gamma \to \tau\tau$ process, the expected precision in the measurement of a_τ would decrease by about 50%. The corresponding constraint at 95% CL is: $-0.0042 < a_\tau < 0.0062$ $(-0.0051 < a_\tau < 0.0072)$. The 68% CL constraint on d_τ is $-1.7 < d_\tau < 1.7 \times 10^{-17} \, e \, \text{cm}$ $(-2.3 < d_\tau < 2.3 \times 10^{-17} \, e \, \text{cm})$, while the 95% CL interval is $-2.9 < d_\tau < 2.9 \times 10^{-17} \, e \, \text{cm}$ $(-3.4 < d_\tau < 3.4 \times 10^{-17} \, e \, \text{cm})$. These results are compared to constraints from other experiments in Fig. 12.

The constraints on a_τ and d_τ can be converted to two-dimensional constraints on the real and imaginary parts of the Wilson coefficients $C_{\tau B}$ and $C_{\tau W}$ divided by Λ^2, using Eq. (5). The 95% CL intervals in the plane of the normalized Wilson coefficients are shown in Fig. 13.

11 Summary

The exclusive photon-induced production of a pair of τ leptons, $\gamma\gamma \to \tau\tau$, has been observed for the first time in proton-proton collisions, with a significance of 5.3 standard deviations (6.5 standard deviations expected). The signal was separated from the inclusive background processes by requiring a low track activity around the di-τ vertex and a low acoplanarity between the τ candidates. The anomalous τ magnetic moment is measured to be $a_\tau = 0.0009^{+0.0032}_{-0.0031}$, while the electric dipole moment of the τ lepton is measured to be $-1.7 < d_\tau < 1.7 \times 10^{-17} \, e \, \text{cm}$.
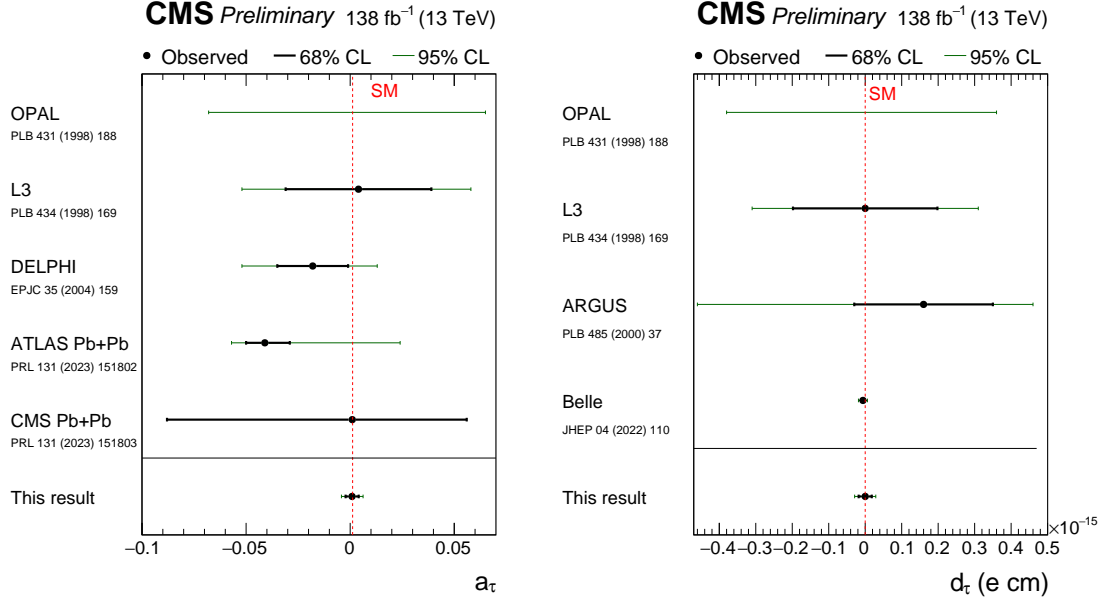
Figure 12: Measurements of a_τ (left) and d_τ (right) performed in this analysis, compared with previous results from the OPAL, L3, ARGUS, Belle, CMS, and ATLAS experiments [12, 13, 15–18]. Confidence intervals at 68 and 95% CL are shown with thick black and thin green lines, respectively.
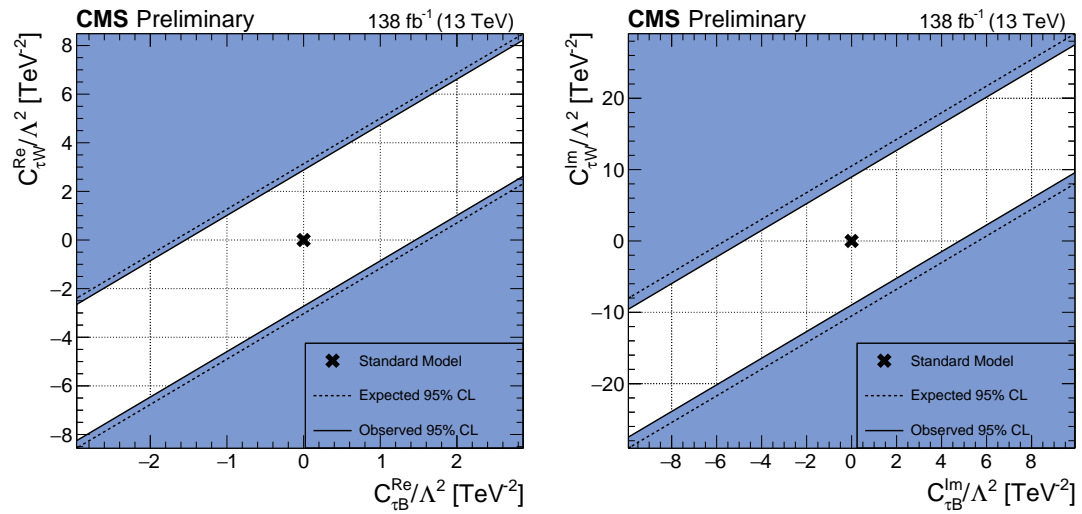

Figure 13: Expected and observed 95% CL constraints on the real (left) and imaginary (right) parts of the Wilson coefficients $C_{\tau B}$ and $C_{\tau W}$ divided by Λ^2. The SM value is indicated with a cross.

References

[1] CMS Collaboration, "Search for exclusive or semi-exclusive photon pair production and observation of exclusive and semi-exclusive electron pair production in pp collisions at $\sqrt{s} = 7$ TeV", *JHEP* **11** (2012) 080, `doi:10.1007/JHEP11(2012)080`, `arXiv:1209.1666`.

[2] CMS Collaboration, "Exclusive photon-photon production of muon pairs in proton-proton collisions at $\sqrt{s} = 7$ TeV", *JHEP* **01** (2012) 052, `doi:10.1007/JHEP01(2012)052`, `arXiv:1111.5536`.

[3] J. Schwinger, "On quantum-electrodynamics and the magnetic moment of the electron", *Phys. Rev.* **73** (1948) 416, `doi:10.1103/PhysRev.73.416`.

[4] R. H. Parker et al., "Measurement of the fine-structure constant as a test of the standard model", *Science* **360** (2018) 191, `doi:10.1126/science.aap7706`, `arXiv:1812.04130`.

[5] X. Fan, T. G. Myers, B. A. D. Sukra, and G. Gabrielse, "Measurement of the electron magnetic moment", *Phys. Rev. Lett.* **130** (2023) 071801, `doi:10.1103/PhysRevLett.130.071801`, `arXiv:2209.13084`.

[6] Muon g-2 Collaboration, "Measurement of the positive muon anomalous magnetic moment to 0.46 ppm", *Phys. Rev. Lett.* **126** (2021) 141801, `doi:10.1103/PhysRevLett.126.141801`, `arXiv:2104.03281`.

[7] Muon g-2 Collaboration, "Measurement of the positive muon anomalous magnetic moment to 0.20 ppm", *Phys. Rev. Lett.* **131** (2023) 161802, `doi:10.1103/PhysRevLett.131.161802`, `arXiv:2308.06230`.

[8] L. Beresford and J. Liu, "New physics and tau $g - 2$ using LHC heavy ion collisions", *Phys. Rev. D* **102** (2020) 113008, `doi:10.1103/PhysRevD.102.113008`, `arXiv:1908.05180`. [Erratum: `doi:10.1103/PhysRevD.106.039902`].

[9] S. Eidelman and M. Passera, "Theory of the tau lepton anomalous magnetic moment", *Mod. Phys. Lett. A* **22** (2007) 159, `doi:10.1142/S0217732307022694`, `arXiv:hep-ph/0701260`.

[10] Y. Yamaguchi and N. Yamanaka, "Large long-distance contributions to the electric dipole moments of charged leptons in the standard model", *Phys. Rev. Lett.* **125** (2020) 241802, `doi:10.1103/PhysRevLett.125.241802`, `arXiv:2003.08195`.

[11] M. Dyndal, M. Klusek-Gawenda, M. Schott, and A. Szczurek, "Anomalous electromagnetic moments of τ lepton in $\gamma\gamma \to \tau^+\tau^-$ reaction in Pb+Pb collisions at the LHC", *Phys. Lett. B* **809** (2020) 135682, `doi:10.1016/j.physletb.2020.135682`, `arXiv:2002.05503`.

[12] ATLAS Collaboration, "Observation of the $\gamma\gamma \to \tau\tau$ process in Pb+Pb collisions and constraints on the τ-lepton anomalous magnetic moment with the ATLAS detector", *Phys. Rev. Lett.* **131** (2023) 151802, `doi:10.1103/PhysRevLett.131.151802`, `arXiv:2204.13478`.

[13] CMS Collaboration, "Observation of τ lepton pair production in ultraperipheral lead-lead collisions at $\sqrt{s_{NN}} = 5.02$ TeV", *Phys. Rev. Lett.* **131** (2023) 151803, `doi:10.1103/PhysRevLett.131.151803`, `arXiv:2206.05192`.

[14] DELPHI Collaboration, "Study of tau-pair production in photon-photon collisions at LEP and limits on the anomalous electromagnetic moments of the tau lepton", *Eur. Phys. J. C* **35** (2004) 159, `doi:10.1140/epjc/s2004-01852-y`, `arXiv:hep-ex/0406010`.

[15] OPAL Collaboration, "An upper limit on the anomalous magnetic moment of the tau lepton", *Phys. Lett. B* **431** (1998) 188, `doi:10.1016/S0370-2693(98)00520-6`, `arXiv:hep-ex/9803020`.

[16] L3 Collaboration, "Measurement of the anomalous magnetic and electric dipole moments of the tau lepton", *Phys. Lett. B* **434** (1998) 169, `doi:https://doi.org/10.1016/S0370-2693(98)00736-9`.

[17] Belle Collaboration, "An improved search for the electric dipole moment of the τ lepton", *JHEP* **04** (2022) 110, `doi:10.1007/JHEP04(2022)110`, `arXiv:2108.11543`.

[18] ARGUS Collaboration, "A search for the electric dipole moment of the tau lepton", *Phys. Lett. B* **485** (2000) 37, `doi:10.1016/S0370-2693(00)00630-4`, `arXiv:hep-ex/0004031`.

[19] ATLAS Collaboration, "Observation of photon-induced W^+W^- production in pp collisions at $\sqrt{s} = 13$ TeV using the ATLAS detector", *Phys. Lett. B* **816** (2021) 136190, `doi:10.1016/j.physletb.2021.136190`, `arXiv:2010.04019`.

[20] CMS Collaboration, "Study of exclusive two-photon production of W^+W^- in pp collisions at $\sqrt{s} = 7$ TeV and constraints on anomalous quartic gauge couplings", *JHEP* **07** (2013) 116, `doi:10.1007/JHEP07(2013)116`, `arXiv:1305.5596`.

[21] CMS Collaboration, "Evidence for exclusive $\gamma\gamma \to W^+W^-$ production and constraints on anomalous quartic gauge couplings in pp collisions at $\sqrt{s} = 7$ and 8 TeV", *JHEP* **08** (2016) 119, `doi:10.1007/JHEP08(2016)119`, `arXiv:1604.04464`.

[22] CMS and TOTEM Collaborations, "Observation of proton-tagged, central (semi)exclusive production of high-mass lepton pairs in pp collisions at 13 TeV with the CMS-TOTEM precision proton spectrometer", *JHEP* **07** (2018) 153, `doi:10.1007/JHEP07(2018)153`, `arXiv:1803.04496`.

[23] ATLAS Collaboration, "Measurement of exclusive $\gamma\gamma \to W^+W^-$ production and search for exclusive Higgs boson production in pp collisions at $\sqrt{s} = 8$ TeV using the ATLAS detector", *Phys. Rev. D* **94** (2016) 032011, `doi:10.1103/PhysRevD.94.032011`, `arXiv:1607.03745`.

[24] CMS Collaboration, "The CMS experiment at the CERN LHC", *JINST* **3** (2008) S08004, `doi:10.1088/1748-0221/3/08/S08004`.

[25] CMS Collaboration, "Performance of the cms level-1 trigger in proton-proton collisions at $\sqrt{s} = 13$ TeV", *JINST* **15** (2020) P10017, `doi:10.1088/1748-0221/15/10/P10017`, `arXiv:2006.10165`.

[26] CMS Collaboration, "The CMS trigger system", *JINST* **12** (2017) P01020, `doi:10.1088/1748-0221/12/01/P01020`, `arXiv:1609.02366`.

[27] H.-S. Shao and D. d'Enterria, "gamma-UPC: automated generation of exclusive photon-photon processes in ultraperipheral proton and nuclear collisions with varying form factors", *JHEP* **09** (2022) 248, `doi:10.1007/JHEP09(2022)248`, `arXiv:2207.03012`.

[28] J. Alwall et al., "The automated computation of tree-level and next-to-leading order differential cross sections, and their matching to parton shower simulations", *JHEP* **07** (2014) 079, `doi:10.1007/JHEP07(2014)079`, `arXiv:1405.0301`.

[29] J. Alwall et al., "MadGraph/MadEvent v4: the new web generation", *JHEP* **09** (2007) 028, `doi:10.1088/1126-6708/2007/09/028`.

[30] R. Frederix and S. Frixione, "Merging meets matching in MC@NLO", *JHEP* **12** (2012) 061, `doi:10.1007/JHEP12(2012)061`, `arXiv:1209.6215`.

[31] L. A. Harland-Lang, M. Tasevsky, V. A. Khoze, and M. G. Ryskin, "A new approach to modelling elastic and inelastic photon-initiated production at the LHC: SuperChic 4", *Eur. Phys. J. C* **80** (2020) 925, `doi:10.1140/epjc/s10052-020-08455-0`, `arXiv:2007.12704`.

[32] I. Brivio, Y. Jiang, and M. Trott, "The SMEFTsim package, theory and tools", *JHEP* **12** (2017) 070, `doi:10.1007/JHEP12(2017)070`, `arXiv:1709.06492`.

[33] I. Brivio, "SMEFTsim 3.0 — a practical guide", *JHEP* **04** (2021) 073, `doi:10.1007/JHEP04(2021)073`, `arXiv:2012.11343`.

[34] P. Artoisenet, V. Lemaitre, F. Maltoni, and O. Mattelaer, "Automation of the matrix element reweighting method", *JHEP* **12** (2010) 068, `doi:10.1007/JHEP12(2010)068`, `arXiv:1007.3300`.

[35] P. Nason, "A new method for combining NLO QCD with shower Monte Carlo algorithms", *JHEP* **11** (2004) 040, `doi:10.1088/1126-6708/2004/11/040`, `arXiv:hep-ph/0409146`.

[36] S. Frixione, P. Nason, and C. Oleari, "Matching NLO QCD computations with parton shower simulations: the POWHEG method", *JHEP* **11** (2007) 070, `doi:10.1088/1126-6708/2007/11/070`, `arXiv:0709.2092`.

[37] S. Alioli, P. Nason, C. Oleari, and E. Re, "A general framework for implementing NLO calculations in shower Monte Carlo programs: the POWHEG BOX", *JHEP* **06** (2010) 043, `doi:10.1007/JHEP06(2010)043`, `arXiv:1002.2581`.

[38] S. Alioli et al., "Jet pair production in POWHEG", *JHEP* **04** (2011) 081, `doi:10.1007/JHEP04(2011)081`, `arXiv:1012.3380`.

[39] S. Alioli, P. Nason, C. Oleari, and E. Re, "NLO Higgs boson production via gluon fusion matched with shower in POWHEG", *JHEP* **04** (2009) 002, `doi:10.1088/1126-6708/2009/04/002`, `arXiv:0812.0578`.

[40] T. Sjöstrand et al., "An introduction to PYTHIA 8.2", *Comput. Phys. Commun.* **191** (2015) 159, `doi:10.1016/j.cpc.2015.01.024`, `arXiv:1410.3012`.

[41] CMS Collaboration, "Extraction and validation of a new set of CMS PYTHIA8 tunes from underlying-event measurements", *Eur. Phys. J. C* **80** (2020) 4, `doi:10.1140/epjc/s10052-019-7499-4`, `arXiv:1903.12179`.

[42] R. D. Ball et al., "Unbiased global determination of parton distributions and their uncertainties at NNLO and at LO", *Nucl. Phys. B* **855** (2012) 153, `doi:10.1016/j.nuclphysb.2011.09.024`, `arXiv:1107.2652`.

[43] NNPDF Collaboration, "Parton distributions with QED corrections", *Nucl. Phys. B* **877** (2013) 290, `doi:10.1016/j.nuclphysb.2013.10.010`, `arXiv:1308.0598`.

[44] NNPDF Collaboration, "Parton distributions from high-precision collider data", *Eur. Phys. J. C* **77** (2017) 663, `doi:10.1140/epjc/s10052-017-5199-5`, `arXiv:1706.00428`.

[45] GEANT4 Collaboration, "GEANT4 — a simulation toolkit", *Nucl. Instrum. Meth. A* **506** (2003) 250, `doi:10.1016/S0168-9002(03)01368-8`.

[46] CMS Collaboration, "Particle-flow reconstruction and global event description with the CMS detector", *JINST* **12** (2017) P10003, `doi:10.1088/1748-0221/12/10/P10003`, `arXiv:1706.04965`.

[47] CMS Collaboration, "Electron and photon reconstruction and identification with the CMS experiment at the CERN LHC", *JINST* **16** (2021) P05014, `doi:10.1088/1748-0221/16/05/P05014`, `arXiv:2012.06888`.

[48] CMS Collaboration, "ECAL 2016 refined calibration and Run2 summary plots", CMS Detector Performance Summary CMS-DP-2020-021, 2020.

[49] CMS Collaboration, "Performance of the CMS muon detector and muon reconstruction with proton-proton collisions at $\sqrt{s} = 13$ TeV", *JINST* **13** (2018) P06015, `doi:10.1088/1748-0221/13/06/P06015`, `arXiv:1804.04528`.

[50] CMS Collaboration, "Performance of reconstruction and identification of τ leptons decaying to hadrons and ν_τ in pp collisions at $\sqrt{s} = 13$ TeV", *JINST* **13** (2018) P10005, `doi:10.1088/1748-0221/13/10/P10005`, `arXiv:1809.02816`.

[51] CMS Collaboration, "Identification of hadronic tau lepton decays using a deep neural network", *JINST* **17** (2022) P07023, `doi:10.1088/1748-0221/17/07/P07023`, `arXiv:2201.08458`.

[52] CMS Collaboration, "Performance of missing transverse momentum reconstruction in proton-proton collisions at $\sqrt{s} = 13$ TeV using the CMS detector", *JINST* **14** (2019) P07004, `doi:10.1088/1748-0221/14/07/P07004`, `arXiv:1903.06078`.

[53] CMS Collaboration, "Description and performance of track and primary-vertex reconstruction with the CMS tracker", *JINST* **9** (2014) P10009, `doi:10.1088/1748-0221/9/10/P10009`, `arXiv:1405.6569`.

[54] CMS Tracker Group Collaboration, "The CMS phase-1 pixel detector upgrade", *JINST* **16** (2021) P02027, `doi:10.1088/1748-0221/16/02/P02027`, `arXiv:2012.14304`.

[55] CMS Collaboration, "Track impact parameter resolution for the full pseudo rapidity coverage in the 2017 dataset with the CMS phase-1 pixel detector", CMS Detector Performance Summary CMS-DP-2020-049, 2020.

[56] CMS Collaboration, "Precision luminosity measurement in proton-proton collisions at $\sqrt{s} = 13$ TeV in 2015 and 2016 at CMS", *Eur. Phys. J. C* **81** (2021) 800, `doi:10.1140/epjc/s10052-021-09538-2`, `arXiv:2104.01927`.

[57] CMS Collaboration, "CMS luminosity measurement for the 2017 data-taking period at $\sqrt{s} = 13$ TeV", CMS Physics Analysis Summary CMS-PAS-LUM-17-004, 2018.

[58] CMS Collaboration, "CMS luminosity measurement for the 2018 data-taking period at $\sqrt{s}$ = 13 TeV", CMS Physics Analysis Summary CMS-PAS-LUM-18-002, 2019.

[59] R. Barlow and C. Beeston, "Fitting using finite Monte Carlo samples", *Comput. Phys. Commun.* **77** (1993) 219, `doi:10.1016/0010-4655(93)90005-W`.

[60] CMS Collaboration, "Measurement of the inelastic proton-proton cross section at $\sqrt{s} = 13$ TeV", *JHEP* **07** (2018) 161, `doi:10.1007/JHEP07(2018)161`, `arXiv:1802.02613`.